Straining soft colloids in aqueous nematic liquid crystals

Peter C. Mushenheim,[a] Joel S. Pendery,[a] Douglas B. Weibel*[b] Saverio E. Spagnolie*[c] and Nicholas L. Abbott*[a]

[a]*Department of Chemical and Biological Engineering, University of Wisconsin-Madison, 1415 Engineering Drive, Madison, WI, 53706, USA. Fax: +1 608-262-5434; Tel: +1 608-265-5278*
[b]*Department of Biochemistry, University of Wisconsin-Madison, 433 Babcock Drive, Madison, WI, 53706, USA*. Fax: +1 608-265-0764; Tel: +1 608-890-1342
[c]*Department of Mathematics, University of Wisconsin-Madison, 480 Lincoln Drive, Madison, WI, 53706, USA*. Fax: +1 608-263-8891; Tel: +1 608-262-3852

**To whom correspondence can be addressed*: Douglas B. Weibel (weibel@biochem.wisc.edu), Saverio E. Spagnolie (spagnolie@math.wisc.edu) and Nicholas L. Abbott (abbott@engr.wisc.edu)

Supporting Information

Materials: 1,2-dioleoyl-*sn*-glycero-3-phosphocholine (DOPC), 1,2-dioleoyl-*sn*-glycero-3-phosphoethanolamine-N-[methoxy(polyethylene glycol)-2000] (ammonium salt) (DOPE-PEG2000), and 1,2-distearoyl-*sn*-glycero-3-phosphoethanolamine-N-[poly(ethylene glycol)2000-N'-carboxyfluorescein] (ammonium salt) (DSPE-PEG2000-CF) were purchased from Avanti Polar Lipids, Inc. (Alabaster, AL). *N*-(4,4-difluoro-5,7-dimethyl-4-bora-3a,4a-diaza-*s*-indacene-3-propionyl)-1,2-dihexadecanoyl-*sn*-glycero-3-phosphoethanolamine triethylammonium salt (BODIPY-DHPE) was obtained from Molecular Probes (Eugene, OR). Disodium cromoglycate (DSCG) was purchased from Sigma-Aldrich (Milwaukee, WI) and used as received. Chloroform was obtained from Sigma-Aldrich (St. Louis, MO). Fisher's Finest Premium grade glass slides and cover glass and amber glass vials (O.D. = 15 mm) were purchased from Fisher Scientific (Pittsburgh, PA). Deionization of a distilled water source was performed with a Milli-Q system (Millipore, Bedford, MA) to give water with a resistivity of 18.2 MΩ cm.

GUV preparation

A 100 μL solution of a phospholipid mixture (1 mM total lipid concentration) in chloroform was added to the bottom of a small glass vial. The lipid mixtures contained a small amount (0.2 – 2 mol%) of DOPE-PEG2000 (or DSPE-PEG2000-CF) and up to 0.5 mol% of BODIPY-DHPE. The solvent was subsequently evaporated from the lipid mixture using a stream of nitrogen prior to the vial being placed under vacuum for at least 2 h, leaving dried lipid films on the vial walls. The vial was then immersed in a water bath at 48°C. To promote GUV formation, we next performed a pre-incubation step in which 2 μL of water was added to the vial and incubated for 5

minutes. Then 200 μL of 15 wt% DSCG solution (heated into its isotropic phase) was added to the glass vial in the hot water bath. GUVs formed over the course of an incubation period of at least 1.5 h. Care was taken to minimize agitation of the vial during this incubation step to maximize GUV yield. Consistent with a previous report (16), we found that our GUV yield was significantly improved when PEG-lipids, which facilitate GUV formation by promoting steric repulsions between lipid layers deposited on the glass vial, were included in the lipid mixture.

Microscopy: GUVs prepared in 15 wt% DSCG were imaged using an Olympus IX71 inverted microscope equipped with a 100× oil-immersion objective, a 60× objective, crossed polarizers, and a 100W mercury lamp. Bright field, polarized light, and fluorescence micrographs of the GUVs were collected with a Hamamatsu 1394 ORCAER CCD camera (Bridgewater, NJ) connected to a computer and controlled through SimplePCI imaging software (Compix, Inc., Cranberry Twp., NJ). BODIPY and carboxyfluorescein fluorescence were both imaged using a fluorescence filter cube with an excitation filter of 480 nm and an emission filter of 535 nm. An Olympus BX60 microscope equipped with crossed polarizers was also used to image DSCG samples. Images were captured using a digital camera (Olympus C-2040 Zoom) mounted on the microscope and set to an f-stop of 2.8 and a shutter speed of 1/25 s. The GUVs imaged in our study were located at the mid-plane of the optical cell (with thickness 60 μm), and were observed to be moving (via diffusion or convection). We did not image vesicles that were near the surfaces of the optical cell.

GUV shape and lipid/fluorophore composition

We measured an approximately uniform fluorescence signal from the lipid bilayers of most GUVs, in both nematic and isotropic DSCG, suggesting that the fluorescent probe is homogenously dispersed in the bilayer. As noted in the main text, we also observed some bright regions in some GUVs (**Fig. S1**), although we do not believe that they are caused by a phase separation of lipids in the GUVs.

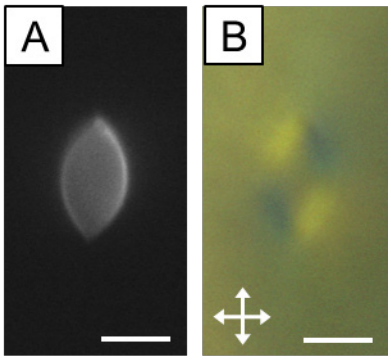

Fig. S1. (A, B) Fluorescence and crossed polars micrographs, respectively, of a DOPC/DSPE-PEG-2000-CF GUV in nematic 15 wt% DSCG at 25ºC. We observed the lipid bilayer of each GUVs prepared with this lipid mixture to exhibit a uniform fluorescence signal, suggesting that PEG-lipids do not phase separate within the bilayers. Scale bars = 5 μm.

We note that the method we used to hydrate the lipid resulted in a polydisperse population of spherical GUVs in isotropic DSCG. The sizes and shapes of GUVs in 15 wt% DSCG at 48°C were similar to those of GUVs that we prepared in other isotropic solutions, such as water and 5.5 wt% DSCG (**Fig. S2**). We also note that we observed a smaller fraction of vesicles to adopt non-spherical shapes in the isotropic solution or to possess "onion-like" structures (**Fig S3-S5**), as compared to our observations in nematic DSCG. In this paper, however, we focus on results obtained with unilamellar vesicles exhibiting spherical shapes in isotropic DSCG and their products in nematic DSCG.

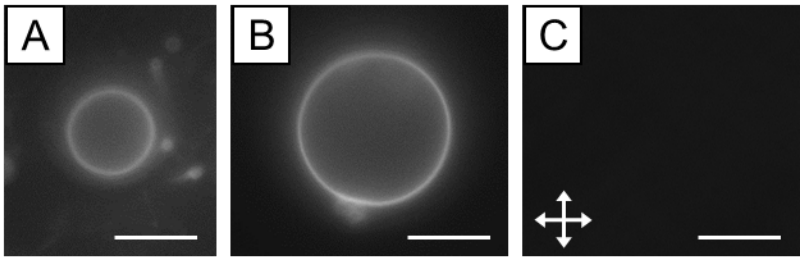

Fig. S2. GUVs prepared in isotropic solutions at 25ºC. (A) Fluorescence micrograph of a DOPC/DOPE-PEG2000/BODIPY-DHPE GUV in water. (B, C) Fluorescence and crossed polars micrographs, respectively, of a DOPC/DOPE-PEG2000/BODIPY-DHPE GUV in 5.5 wt% DSCG. Scale bars = 10 μm.

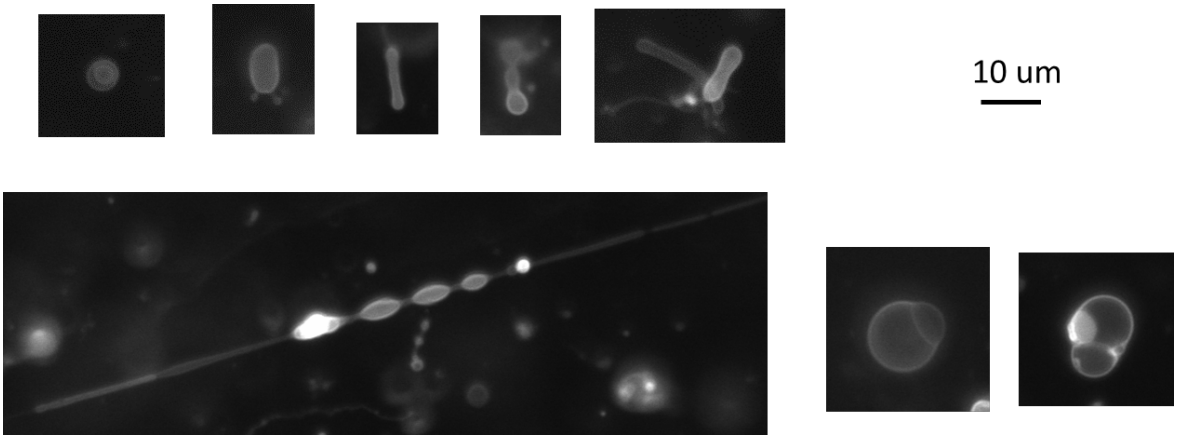

Fig. S3. Examples of non-spherical GUVs in isotropic 15 wt% DSCG at 50ºC.

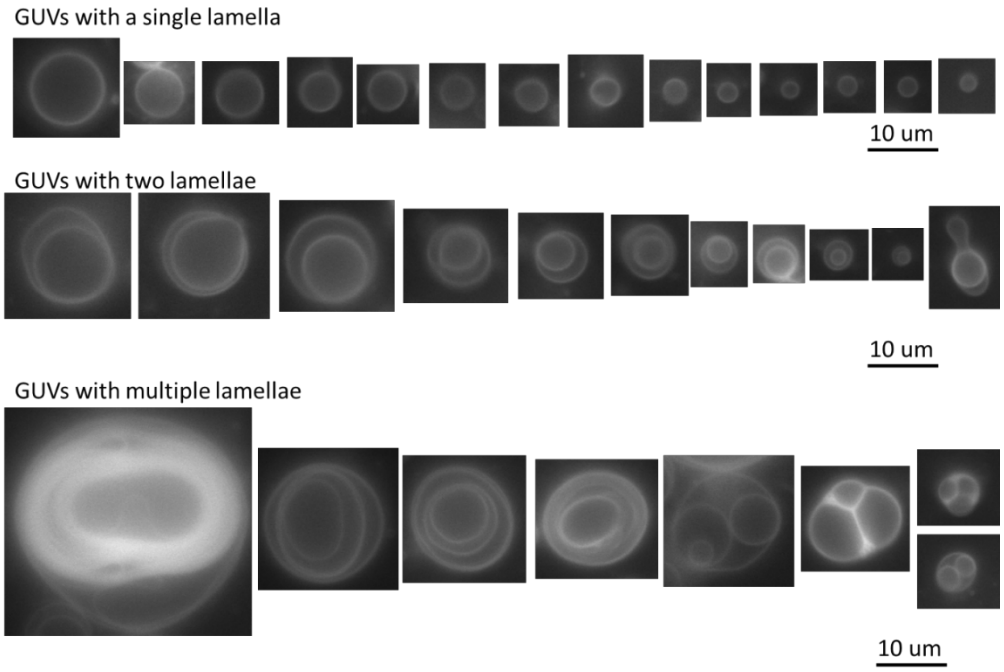

Fig. S4. Examples of spherical unilamellar GUVs as well as vesicles exhibiting "onion-like" structures in DI water at 25ºC.

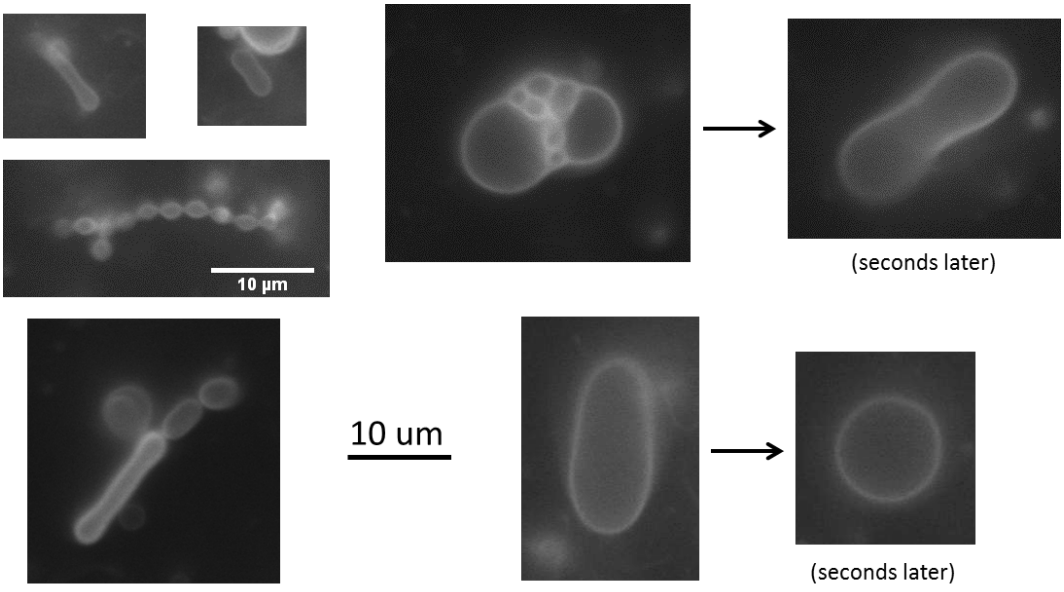

Fig. S5. Examples of non-spherical GUVs prepared in DI water at 25ºC.

GUVs in isotropic 15 wt% DSCG at 50ºC

Prior to quenching experimental samples containing vesicles formed in 15 wt% DSCG solution from 50ºC to 25ºC, in addition to vesicles that were spherical in shape, we observed non-spherical vesicles as well as vesicles that possessed more than one lamellae (**Fig. S3**). Such non-spherical vesicles were also observed in other isotropic solutions, such as pure water (**Fig. S4,S5**). Included in the diverse GUV shapes we observed were slightly elongated prolate and oblate GUVs, fused GUVs comprised of multiple compartments, and tubular membranes (that we occasionally observed to exhibit pearling instabilities(39)). Moreover, the membranes of these non-spherical GUVs are "floppy" and exhibit dynamic undulations and shape changes as a result of thermal fluctuations. Such fluctuating, non-spherical GUVs have been shown to form in isotropic solutions when GUVs possess excess membrane area as a result of osmotic pressure differences or fusion events between multiple GUVs and also when a mismatch exists between the number of lipids comprising the inner and outer leaflets of a lipid bilayer forming a GUV (40, 36). We suspect this apparent diversity of GUV shapes in isotropic 15 wt% DSCG might contribute to the resulting varied landscape of shapes GUVs adopt upon quenching the solution into the nematic phase. For example, we hypothesize that the excess surface area exhibited by non-spherical GUVs in the isotropic phase might lead to the formation of wrinkles (**Fig. 5A-D**) upon quenching to the nematic DSCG phase. We note, however, that it is not exclusively this population of initially non-spherical GUVs that adopts elongated shapes in the nematic LC (see, for example, **Video S1**). In addition, we note that such thermal shape fluctuations were entirely suppressed in GUVs upon quenching into the nematic DSCG phase, consistent with previous studies showing that shape fluctuations vanish upon application of even small (~0.001 mN/m) tensions to GUVs (41).

DSCG composition inside slightly strained GUVs

If GUV volume is conserved during the transformation of spherical GUVs to strained GUVs with $R/r < 1.54$, then there should be no change in composition of the DSCG phase within the GUVs. Accordingly, the temperatures at which phase transitions initiate (nematic/isotropic) should be approximately the same inside and outside each GUV. To test this prediction, we heated GUV-containing DSCG samples from 26ºC to 50ºC at a rate of ~0.5ºC/min (N=5). In **Fig. S6A-F**, we provide an example of the sequence of phase transitions we observed inside and outside a GUV with an initial aspect ratio of $R/r \approx 1.14$ in the nematic phase (**Video S4**). We found that isotropic phase domains nucleated near the surface of GUVs at temperatures approximately 1ºC lower than those at which isotropic domains first appeared in the bulk of the continuous nematic DSCG solution outside of GUVs (N = 5) (**Fig. S6C,D**). (Note that these isotropic domains do not appear dark between crossed polarizers due to the birefringence of the nematic DSCG outside of the GUVs.) Furthermore, we did not observe any preferrential isotropic nucleation site on the GUV membrane (e.g. at the cusps/poles) in the GUV population studied (N=5). It was difficult for us to determine whether these domains intially formed on the inside and/or the outside of the GUV membrane. Upon heating the sample through the range of temperatures in which nematic and isotropic phase domains coexisted within the DSCG solution inside and outside the GUVs (see later in SI for additional discussion), the GUVs transitioned to spherical shapes (**Fig. S6E,F**).

Upon cooling the sample from 50ºC (**Fig. S6G-L; Video S5**), nematic domains appeared outside of GUVs at temperatures of ≈2.5ºC higher than that at which nematic domains were evident inside the GUVs (N = 4) (**Fig. S6I,J**). Additional cooling of the sample led to the growth of

nematic phase domains both inside and outside of GUVs (see later in SI for additional discussion) followed by the eventual disappearance of remaining isotropic phase domains (**Fig. S6K,L**). We note that we also occasionally observed coexistence between isotropic and columnar phase domains in our samples at temperatures above 41ºC when performing these experiments (42).

The absence of an increase in the phase transition temperature of the DSCG solution internal to the GUVs in these experiments (as compared to the external DSCG solution) suggests that the DSCG concentration inside GUVs is not enriched relative to the outside solution. We hypothesize that the observed shift of phase transitions to lower temperatures inside the GUVs might reflect i) heightened elastic strain associated with confinement of LCs inside GUVs or ii) local depletion of DSCG near the surface of the GUV membrane.

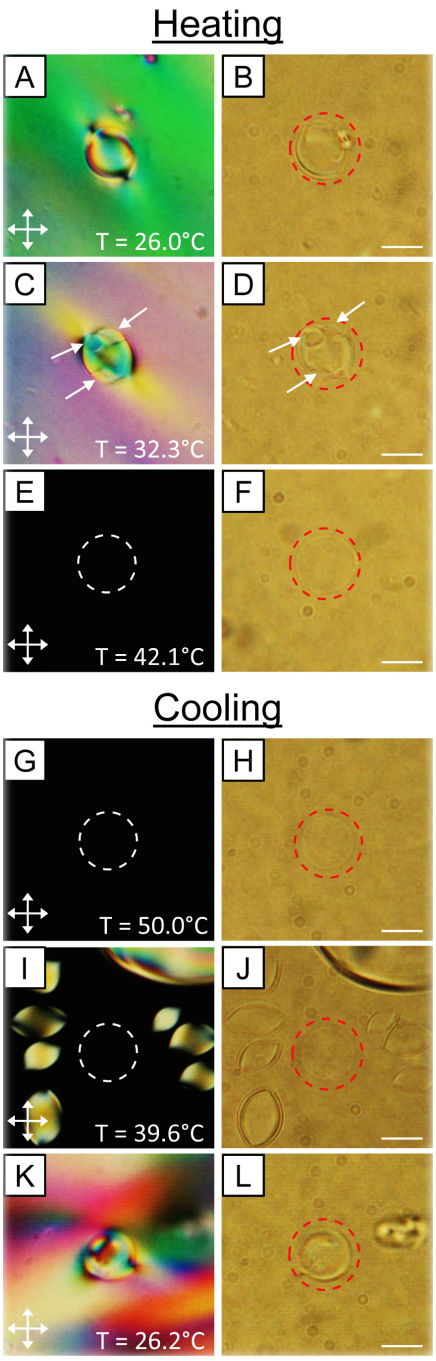

Fig. S6. Characterization of DSCG phase transitions inside and outside of GUVs. Crossed polars and corresponding bright field micrographs obtained while (A – F) heating a GUV-containing sample from 26ºC to 50ºC and (G – L) subsequently cooling the sample from 50ºC to 26ºC at a rate of ~0.5ºC/min. Micrographs were collected at the temperatures indicated in the figure. White dotted lines outline the GUV in crossed polars micrographs when the internal DSCG solution is largely in its isotropic phase while red dotted lines outline the region of the droplet in bright field micrographs to facilitate the location of the droplet edge. In C and D, isotropic phase domains are indicated with arrows. Scale bars = 20 µm.

Quantitative analysis of GUVs shapes

The analysis of the GUVs was performed in MATLAB using a custom analysis script. The image was imported (**Fig. S7a**) and the region with the GUV to be analyzed is selected using a graphical user interface (GUI). The selected GUV is thresholded to perform edge detection and a user drawn line is input on the thresholded image to bisect the GUV from one cusp to the other. Using a GUI, the user may choose to erase regions around the GUV boundary that the threshold was unable to remove due to intensity gradients within the microscope image. High intensity regions that cause overexposure within the image and blur the boundary are masked, if necessary, so that the pixels are not included in the edge data when performing the fit. The boundary of the GUV is then detected, the high intensity masked pixels are removed, and each half of the bisected GUV is fit to a circle, where the center and radius are determined by the fit (**Fig. S7b**). The major and minor axes of the GUV are determined respectively from the point of intersection of the two circles and the points where a line connecting the circle centers intersect with each circle. These lengths are used to calculate the aspect ratio of the GUV. Finally, the cusp angles of the GUV are calculated from the circular fit of the GUV by the angle between the tangent lines of both circles at each intersection point.

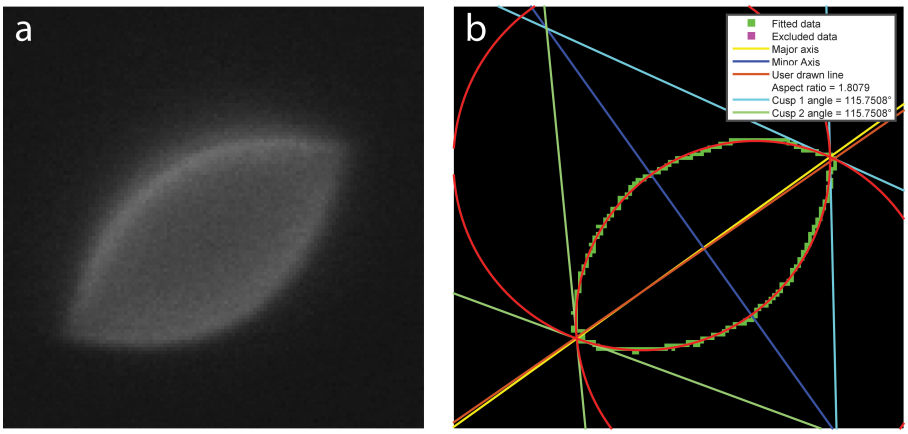

Fig. S7. Quantitative analysis of GUVs. (a) Fluorescence micrograph of a GUV in nematic 15 wt% DSCG and (b) the resulting fit of the GUV perimeter (pixels in green), including both

circular fits (red lines), the user drawn line (orange line), the major and minor axes of the GUV calculated from the circular fits (yellow and blue lines respectively), and the cusp angles calculated as the angle between the light green lines and separately the light blue lines. The aspect ratio is calculated using the major and minor axis lengths of the GUV.

From this analysis, we found that two distinct populations of GUVs formed in our samples: slightly elongated GUVs with rounded poles ($\alpha > 130^{o}$) and highly elongated and cusped GUVs ($\alpha < 130^{o}$) (see main text for details). The GUVs in the population with $\alpha > 130^{o}$ were approximately prolate spheroidal in shape. To quantify the surface area and volume of these GUVs, we used the expressions

$$SA_{\alpha>130^{\circ}} = 2\pi r^2\left[1+\frac{R}{r\delta}\sin^{-1}(\delta)\right] \quad \text{S1}$$

$$V_{\alpha>130^{\circ}} = \frac{4}{3}\pi R r^2 \quad \text{S2}$$

where $\delta^2 = 1-\frac{r^2}{R^2}$. The semi-major axis (R) and semi-minor axis (r) of GUVs were measured using the MATLAB script.

Alternatively, the shapes of GUVs in the population with $\alpha < 130^{o}$ were best described as bodies of revolution of parabolic curves. Thus, we quantified the surface area and volume of these GUVs using the expressions

$$SA_{\alpha<130^{\circ}} = \frac{\pi}{16r^2}\left[2r(8r^2-R^2)\sqrt{4r^2+R^2}+(16r^2R^2+R^4)\sinh^{-1}\left(\frac{2r}{R}\right)\right] \quad \text{S3}$$

$$V_{\alpha<130^{\circ}} = \frac{16}{15}\pi R r^2 \quad \text{S4}$$

where R and r are again the semi-major and semi-minor axis of GUVs, respectively.

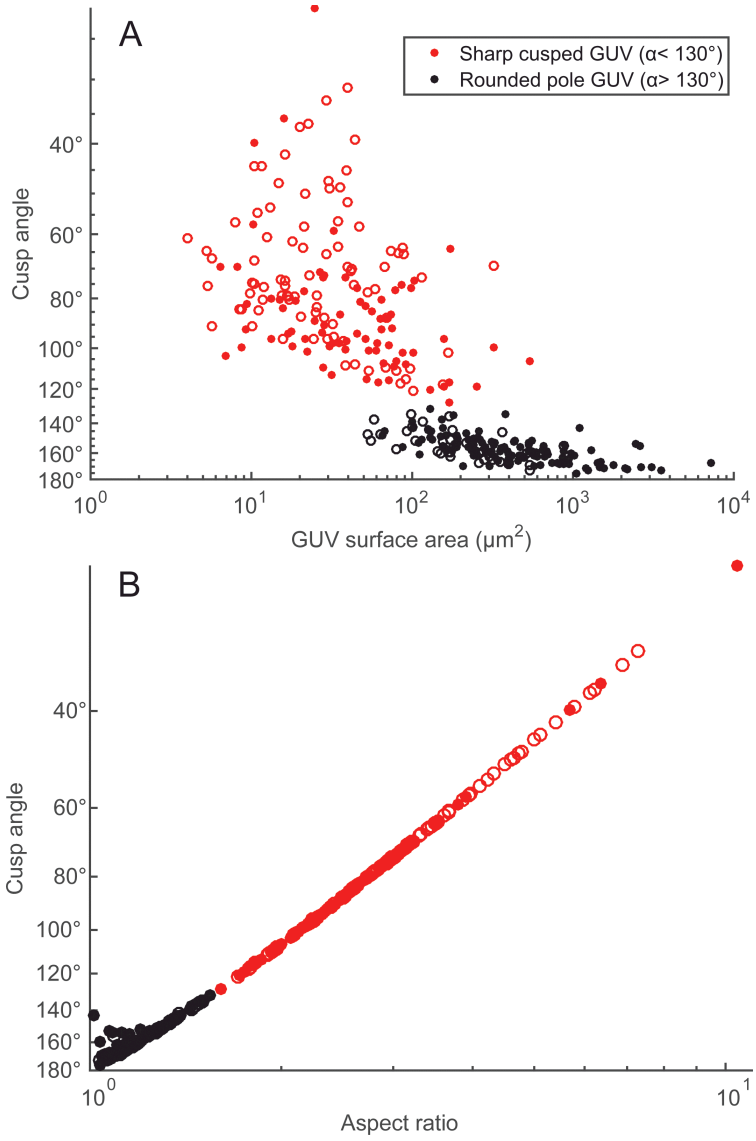

Fig. S8. Plot of A) GUV cusp angle (α) as a function of A) surface area and B) aspect ratio for GUVs in nematic 15 wt% DSCG. Data in red denote GUVs with cusp angles $\alpha < 130^{\circ}$ and data in black denote GUVs with cusp angles $\alpha > 130^{\circ}$. Filled points denote GUVs containing 2 mol% PEG-lipid and unfilled points denote GUVs containing 0.2 mol% PEG-lipid.

Observations of GUV-containing samples at temperatures within the two-phase coexistence range of DSCG

In **Fig. S9**, additional micrographs collected at temperatures within the two-phase nematic-isotropic coexistence range during temperature ramp and quench experiments (**Fig. S6**) are presented. During the heating of the GUV-containing sample, following the nucleation of isotropic domains near the surface of a GUV membrane (**Fig. S6C,D**), isotropic domains subsequently also appeared within the bulk of the continuous DSCG phase. As these isotropic domains grew in size, we found GUVs to be pushed along by the advancing nematic-isotropic interfaces of the domains (**Fig. S9A,B**). Interestingly, as we continued to increase the temperature within the two phase coexistence range of DSCG, we frequently observed a circular disc-shaped nematic domain to form inside of GUVs separating two isotropic domains (**Fig. S9C,D**) prior to the DSCG solution throughout the sample transitioning to the isotropic phase (**Fig. S6E,F**). The localization of the isotropic phase near the poles is consistent with the effects of strain within the nematic phase.

Upon cooling the sample, nematic domains nucleated inside GUVs (**Fig. S9E,F**) at temperatures approximately 2.5ºC lower than outside of the GUVs (**Fig. S6I,J**). As the temperature of the sample was further lowered, the nematic phase domains grew inside and outside of the GUVs (**Fig. S9G,H**) until no isotropic domains remained (**Fig. S6K,L**).

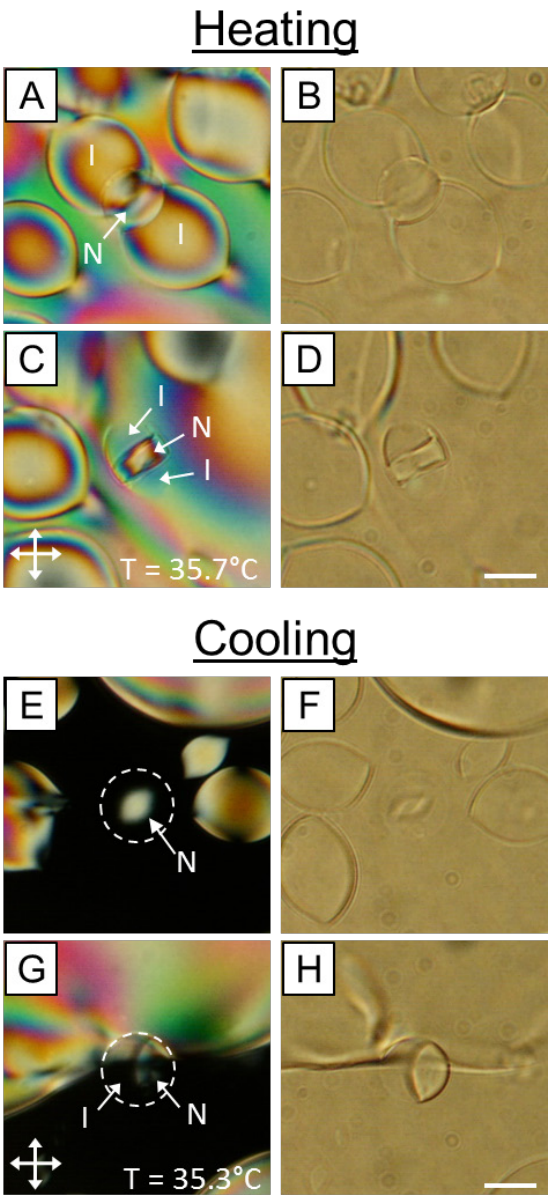

Fig. S9. Crossed polars and corresponding bright field micrographs of a GUV-containing sample obtained at temperatures within the two-phase nematic-isotropic coexistence range of DSCG. Micrographs were collected at the temperatures indicated in the figure while (A – D) heating the sample from 26ºC to 50ºC and (E – H) subsequently cooling the sample from 50ºC to 26ºC at a rate of ~0.5ºC/min. Dotted lines outline the GUV in crossed polars micrographs when the internal DSCG solution is largely in its isotropic phase. The phase (nematic (N) or isotropic (I)) of selected DSCG domains is indicated in the figure. Scale bars = 20 µm.

Numerical solution of the Ericksen-Leslie equations

Consider an axially symmetric model GUV which is parameterized by an arc-length variable $s \in [0, a]$ and a polar angle $\eta \in [0,2\pi]$: $\mathbf{X}(s,\eta) = x(s)\hat{\mathbf{x}} + f(s)\,\hat{\mathbf{r}}(\eta)$, with $\hat{\mathbf{r}}(\eta) = \cos\eta\,\hat{\mathbf{y}} + \sin\eta\,\hat{\mathbf{z}}$ in a cylindrical polar coordinate system with $r = \sqrt{y^2 + z^2}$ and $\eta = \tan(z/y)$. A local tangent angle $\alpha(s)$ is defined implicitly by $\mathbf{X}_s = \cos\alpha(s)\,\hat{\mathbf{x}} + \sin\alpha(s)\;\hat{\mathbf{r}}(\eta)$. The membrane is immersed in a nematic LC. To compute the elastic energy stored in the bulk fluid at equilibrium we study the single-constant approximation of the Frank elastic free energy density (43), which depends on derivatives of the local nematic director field $\hat{\mathbf{n}}(x)$,

$$\mathcal{W}(\hat{\mathbf{n}}) = \frac{K}{2}(\nabla\cdot\hat{\mathbf{n}})^2 + \frac{K}{2}(\hat{\mathbf{n}}\cdot\nabla\times\hat{\mathbf{n}})^2 + \frac{K}{2}|\hat{\mathbf{n}}\times(\nabla\times\hat{\boldsymbol{n}})|^2. \qquad \text{S5}$$

The three terms correspond to elastic costs to splay, twist, and bend the nematic, respectively, and the total energy in the bulk is $\mathcal{E}_F = \int_{\mathbb{R}^3}\mathcal{W}\,d\mathbf{x}$. We assume that the director field is twist-free, and write $\hat{n} = \cos(\theta)\,\hat{\mathbf{x}} + \sin(\theta)\,\hat{\mathbf{r}}(\eta)$ with $\theta(x,r) \in [0,\pi]$.

To the energy functional we add a surface energy to penalize departures from tangential molecular anchoring along the long axis of the immersed GUV with anchoring strength $\mathcal{W}$, given by $\mathcal{E}_S = \int_{\partial\Omega}\mathcal{F}_S\,dS = (W/2)\int_{\partial\Omega}\sin^2(\alpha-\theta)\,dS$, where the integration is performed over the membrane surface and α is the previously defined local tangent angle. To compute the total free elastic energy in the system it is convenient to combine both the bulk and surface terms together into a single volume integral,

$$\mathcal{E} = \int_\Omega \left\{ \frac{K}{2}(\nabla \cdot \hat{\mathbf{n}})^2 + \frac{K}{2}(\hat{\mathbf{n}} \cdot \nabla \times \hat{\mathbf{n}})^2 + \frac{K}{2}|\hat{\mathbf{n}} \times (\nabla \times \hat{\mathbf{n}})|^2 + \mathcal{F}_S \delta(\mathrm{x} - \mathbf{X}) \right\} dV, \quad \text{S6}$$

where the delta function is defined such that

$$\int_\Omega f(\mathrm{x}) \delta(\mathrm{x} - \mathbf{X}) dV = \int_{\partial\Omega} f(\mathbf{X}) dS, \quad \text{S7}$$

In practice we replace δ by a smoothed delta function δ_h with finite but compact support. The form of δ_h used is that derived by Peskin for the classical immersed boundary method (see (44)). To find the equilibrium configuration of the nematic field for a given immersed GUV shape we appeal to the principle of virtual work and compute the variational derivative of $\mathcal{E}$ with respect to the angle field θ, resulting in an equation which must be satisfied at equilibrium,

$$\nabla_r^2 \theta - \frac{\sin(2\theta)}{r^2} + \frac{w}{2} \int_{\partial\Omega} \sin(\alpha(\mathbf{X}) - \theta)\, \delta_h(\mathrm{x} - \mathbf{X}) dS = 0, \quad \text{S8}$$

$$\theta(x, r = 0) = 0, \qquad \theta\left(\sqrt{x^2 + r^2} \to \infty\right) = 0, \quad \text{S9}$$

where $\nabla_r^2 = \partial_{xx} + \partial_{rr}$. The equations have here been made dimensionless by scaling lengths upon the major axis length of the GUV, R, and defining the relative anchoring strength $w = WR/K$.

To solve this nonlinear equation we discretize θ on a regular grid in (x, r), writing $\theta_{ij} = \theta(-3 + 6i/N, 4j/N)$, with $i, j = 0,1, \ldots, N$, and use a second order centered finite difference approximation to the Laplacian operator ∇_r^2. The angle field is set to zero at the boundary of the computational domain implied in the definition of θ_{ij}. Choosing $N = 64$ is

generally sufficient to render discretization errors negligible. Newton iteration is then used to solve Eqn S8. The Jacobian required for Newton iteration is computed using a finite difference approximation at the first iterative step, and then subsequently by a fast Jacobian updating ("good" Broyden's method) (45).

We consider model GUV membranes with prolate ellipsoidal profiles, $r(s) = r_0\sqrt{1-x(s)^2}$, with $x(s) \in [-1,1]$, $\alpha(s) = \tan^{-1}(r_s/x_s)$, and $r_0 \in [0,1]$. Small regions near $x = \pm 1$ of dimensionless radius r_c are treated as cores which are relaxed to zero elastic energy; this is where "boojum" singularities in the nematic are known to appear for sufficiently large anchoring strengths (46). Other defects are also expected to appear in the bulk for large anchoring strengths (8), which we do not pursue here. The choice of core radius size does not have a dramatic effect on the results of the simulations. For example, **Fig. S10a** shows the equilibrium director field configuration inside and outside of a spindle shaped membrane with aspect ratio $r_0 = 0.6$; the relative anchoring strength is $w = 100$ and the dimensionless core radius is $r_c = 0.05$. In our calculation, the director on either side of the membrane is continuous and the "anchoring" in Equation S8 is treated as a field located with support on the membrane surface. In reality, the membrane separates the inner and outer volumes of DSCG and the director field need not be continuous across the interface.

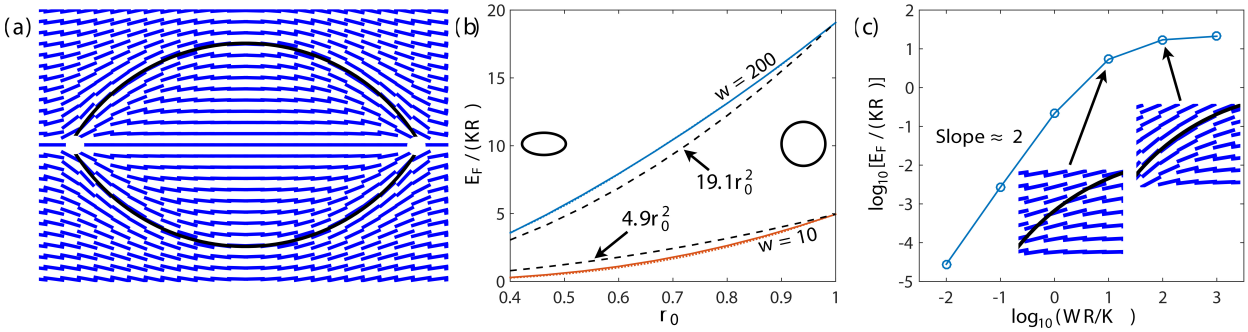

Fig. S10. (a) Equilibrium axisymmetric, twist-less director field around a spindle-shaped

(parabolic profile) body with aspect ratio 0.6, relative anchoring strength $w = WR/K = 100$, and removed cores of radius $r_c = 0.05$. (b) Bulk elastic energy associated with prolate spheroidal membranes (solid lines) and spindles (dotted lines, nearly indistinguishable from the solid lines) with aspect ratio r_0 for $w = 10$ and $w = 200$, with $r_c = 0.05$. Simple estimates Cr_0^2 which match the numerical values for spherical bodies ($r_0 = 1$) are included as dashed lines. (c) Bulk elastic energy as a function of relative anchoring strength w for spherical bodies. The scaling is quadratic with the anchoring strength w for small w. This is also the value of C in the simple estimate $\mathcal{E}_F/(KR) \approx Cr_0^2$ (taking values from 0 to 21 in the range of *w* shown).

In **Figure S10b** we show the bulk energy for two relative anchoring strengths, $w = 10$ and $w = 200$ (with w=WR/K the relative anchoring strength) for prolate spheroidal shells of varying aspect ratio and core radius size r_c=0.05. Spindle-shaped membranes with parabolic profiles of the same aspect ratios were also considered; the associated bulk energies are shown as dotted lines which are nearly indistinguishable from those associated with the prolate spheroidal membranes. Also plotted as dashed lines are the curves $4.9r_0^2$ and $19.1r_0^2$, which are simple estimates for these two anchoring strengths which match the numerical data for the spherical membrane shapes. The expression $\mathcal{E}_F/(KR) \approx Cr_0^2$ is used in the main text when balancing elastic energy with estimates of the surface tension energy, where C depends on the anchoring strength. The present calculation confirms the quadratic scaling of the LC elastic energy with the aspect ratio for nearly spherical GUV shapes. **Figure S10c** shows the total bulk energy associated with spherical vesicles as a function of the relative anchoring strength (which is also the value of C for a given anchoring strength). The dependence of C on the anchoring strength scales as w^2 for small w and begins to plateau after $w \approx 100$. Although the value of the constant C depends on the anchoring strength (it varies from 0 to 21 in the range of *w* shown), its value does not have a sizeable effect on the conclusions described in the main text: different values of C merely shift the dataset up or down in **Fig. 4A** but the slope, which corresponds to how the interfacial tension changes as the surface area changes, is not modified. Following the

suggestions in Refs. (30, 47) we estimate using $R \approx 10\mu m$ that $w \approx 12.5$, and then from **Fig. S10c**, that $C \approx 6$. See also: Refs. (8, 23, 19, 48).

Although not reported in detail here, we have also pursued a more general optimization question, balancing membrane stretching and bending energy against the bulk elastic energy to find the energy minimizing membrane shape. The numerical method described above is a natural one for studying such free boundary problems. For sufficiently small membranes the bending energy dominates and results in the prediction of a spherical membrane shape, so that as size increases we would expect a non-monotonic flow from spherical, to elongated, and then again to spherical GUV shapes. However, for the relatively large GUVs considered in the experiments we expect such effects due to membrane bending energy to be vanishingly small. Specifically, we do not include the membrane bending energy in our calculations reported herein as it scales as $E_B \propto B \approx 10 - 40\ pN\ nm$ (49), where B is a bending stiffness (a function of the elastic modulus and membrane geometry), and is dominated by the elastic LC energy that scales as $E_{LC} \propto KR \approx 10^4 - 10^5\ pN\ nm$. Other extensions of the numerical method have also been pursued, and will appear as a separate paper.

DSCG inside and outside GUVs

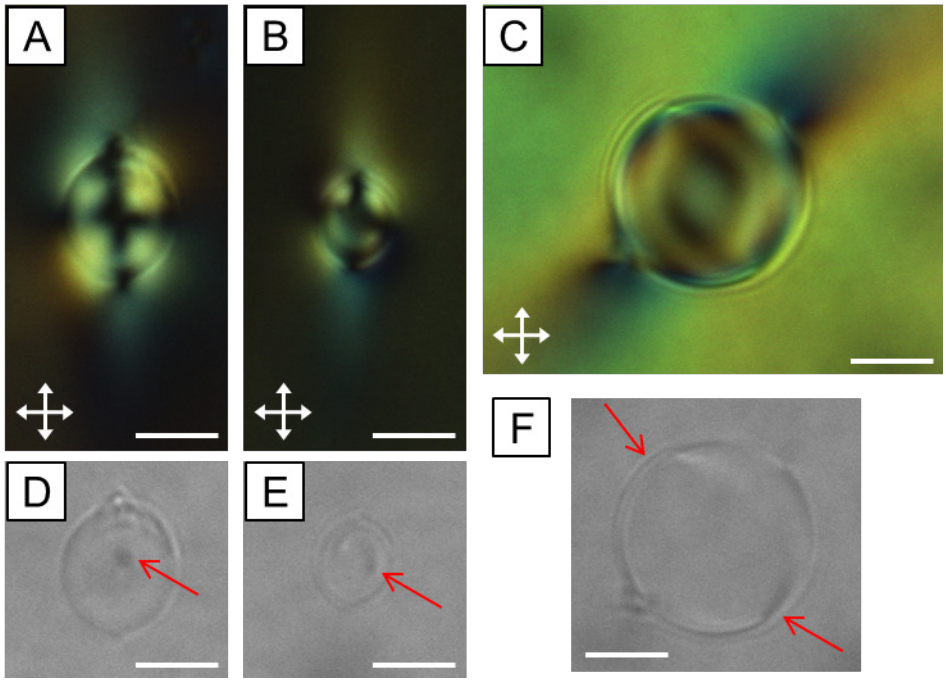

Fig. S11. Configuration of nematic DSCG inside and outside of slightly elongated GUVs ($\alpha >$ 130º). (A – C) Crossed polars micrographs and (D – F) corresponding bright field micrographs of slightly elongated GUVs in nematic 15 wt% DSCG at 25ºC. Boojums are indicated in the bright field images using arrows. Scale bars = 10 µm.

GUVs without PEG-lipid

We hypothesized that depletion of DSCG near membrane surfaces might be promoted in our experiments by the presence of PEG-lipids within the lipid bilayer, as a previous study has reported that the addition of PEG to bulk DSCG solutions leads to condensation of higher order DSCG domains at a given temperature compared to DSCG solutions without PEG (33). Condensation of these domains was attributed to depletion interactions, as PEG molecules likely become expelled from high order DSCG phases. To test this hypothesis, we created GUVs from lipid mixtures that did not contain any PEG-lipids (99.5 mol% DOPC/0.5 mol% BODIPY-DHPE). Although the yield of GUVs was very low in these nematic 15 wt% DSCG samples, the few GUVs we did observe all had $\alpha < 130º$. Moreover, the values of τ_{exp} calculated with Eqn 4

for these GUVs with 0 mol% PEG-lipid were approximately independent of R/r with values of ~ 0.01 mN/m, similar to what we measured for GUVs containing PEG-lipids (**Fig. 4B**).

Director configuration outside and inside of an elongated, highly cusped GUV

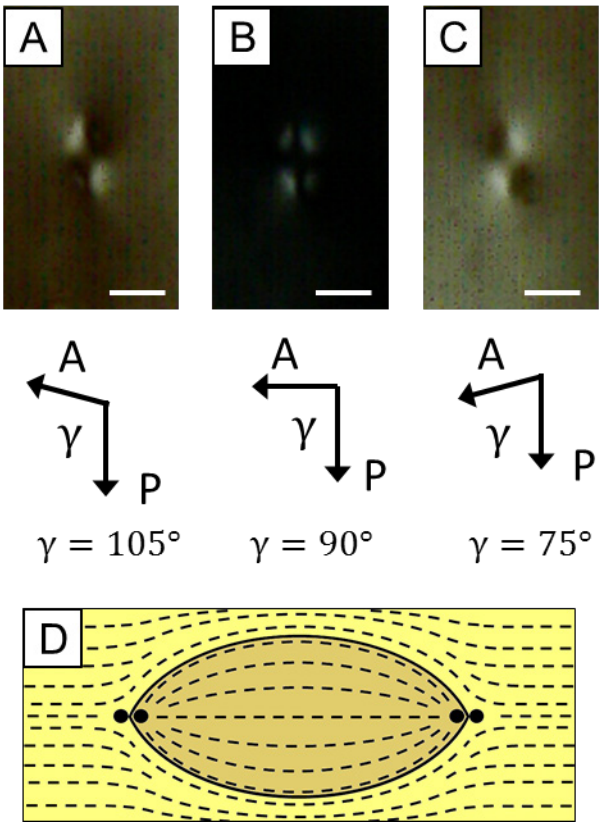

Fig. S12. Characterization of GUVs with $\alpha < 130^{o}$. (A – C) Polarized light micrographs of a GUV in which the angle between the polarizer and the analyzer is varied. (D) Schematic depicting the orientation of the LC inside and outside elongated and cusped GUVs. Scale bars = 5 μm.

To provide insight regarding the LC elastic stresses acting on highly elongated GUVs with $\alpha < 130^{o}$, we characterized the configurations of the nematic DSCG phases inside and outside these GUVs (**Fig. S12**). Whereas pronounced birefringent tails were found extending from the approximately rounded poles of GUVs with $\alpha > 130^{o}$ in the surrounding nematic LC, we did not observe this same optical signature in polarized light micrographs of highly elongated and

cusped GUVs (**Fig. S12A-C**). In fact, there typically were no discernable distortions in the continuous DSCG phase, suggesting that due to the slender shape of these GUVs and the tangential anchoring condition, the nematic DSCG outside the GUV is forced to deviate minimally away from the orientation of the far-field director. We note that Nych, et al. also did not observe distortions of a nematic DSCG phase outside small (< 2 μm diameter) spherical inclusions (14).

We expected that inside the elongated and cusped GUVs, nematic DSCG would adopt a configuration similar to that previously observed in nematic tactoids. Almost exclusively, nematic tactoids have been reported to adopt a bipolar configuration with boojum defects located at the cusped poles (30, 9, 22), although one report of a twisted configuration appearing in sessile tactoids exists (50). In order to determine whether the LC inside these GUV twists, we collected polarized light micrographs with the polarizers oriented at various angles relative to each other and observed the intensity of light transmission in the center of the GUV (**Fig. S12A-C**). Consistent with an internal untwisted bipolar DSCG configuration, we only observed extinction of the light in this central region when the polarizers were set at 90 degrees relative to one another (**Fig. S12B**) (50). Given that we did not observe twist distortions in the more nearly spherical GUVs above, this result is in agreement with the theoretical calculation of Prinsen and van der Schoot that twist distortions are less likely to develop in elongated, tactoid-shaped droplets than in spherical droplets of the same size (48). We also note that we did not observe boojum defects positioned along the minor axis in bright field micrographs of these elongated and cusped GUVs as we did in the case of GUVs with approximately rounded poles. Based on

these results, we conclude that nematic DSCG adopts configurations inside and outside these GUVs as depicted schematically in **Fig. S12D**.

Discussion

Our results indicate that two distinct populations of GUVs form in the nematic DSCG phase. We hypothesize that these two populations might emerge depending on whether or not elastic stresses imparted by the LC are sufficient in magnitude to lead to partial rupture and transient formation of pores in the GUVs.

The population of slightly elongated GUVs characterized by cusp angles of $\alpha > 130^{o}$ appears to form via a process involving the expansion of GUV surface area due to elastic stresses upon quenching from the isotropic to the nematic phase of DSCG while the GUV maintains constant volume. Given this hypothesis, we expected the equilibrium shapes of GUVs within this population in the nematic LC phase to reflect interplay between bulk LC elastic energy and the energy associated with stretching an elastic GUV membrane. However, our analysis of τ_{exp} revealed it to be only a weak function of the fractional surface area expansion ε_{SA} (**Fig. 4A**). Given this result, the energetic coupling appearing to underlie the shapes adopted by GUVs in this population seems to more closely resemble that which leads to the formation of elongated nematic tactoids in lyotropic LCs – coupling between LC elastic energy and a surface energy due to interfacial tension. We hypothesize that this unexpected result could be a consequence of local depletion of DSCG from the region near the surface of GUV membranes, although we note that our analysis suggests that this depletion is not induced solely as a result of the presence of PEG-lipids.

On the other hand, our results suggest that the population of GUVs with $\alpha < 130^{o}$ likely forms through a process in which GUVs partially rupture due to high levels of strain within the membrane imparted by the nematic DSCG phase, allowing 15 wt% DSCG solution to efflux from the GUVs through transient pores in the membrane. This process allows GUVs to adopt highly elongated shapes that give rise to configurations of confined nematic DSCG that are distinct from those observed in the population of GUVs with $\alpha > 130^{o}$. Several experimental observations support this hypothesis, including our measurement that the elastic energy penalty associated with stretching a GUV membrane grows to become comparable to the surface energy arising due to interfacial tension for the smallest and most highly deformed GUVs in the population with $\alpha > 130^{o}$ (**Fig. 4A**). Additionally, our analysis suggests that following the efflux of 15 wt% DSCG solution, the equilibrium shapes adopted by the population of highly elongated and cusped GUVs are influenced by the same balance between LC elastic energy and surface energy arising due to interfacial tension that sets the shapes of the population of GUVs with $\alpha > 130^{o}$ (**Fig. 4B**). We note that although this coupling is reminiscent of that which gives rise to the equilibrium shape of nematic tactoids dispersed in continuous isotropic phases in lyotropic LCs, we measure the aspect ratios of GUVs in our system to vary more dramatically as a function of GUV size than what has been reported for nematic tactoids. Specifically, whereas a recent study reports the aspect ratios of tactoids that form in dispersions of carbon nanotubes in chlorosulfonic acid to vary between 2 and 6 for tactoids characterized by major axes ranging from 5 to 200 μm in length (51), in our system we measure the aspect ratios of GUVs to vary between 1 and 10 for GUVs with major axis lengths between 2.5 μm and 50 μm.

References

1. Aida T, Meijer EW, Stupp SI (2012) Functional supramolecular polymers. *Science (80-)* 335(6070):813–817.
2. Renner LD, Weibel DB (2011) Cardiolipin microdomains localize to negatively curved regions of Escherichia coli membranes. *Proc Natl Acad Sci U S A* 108(15):6264–6269.
3. Wang N, Butler JP, Ingber DE (1993) Mechanotransduction across the cell surface and through the cytoskeleton. *Science (80-)* 260(5111):1124–1127.
4. Petka WA, Harden JL, McGrath KP, Wirtz D, Tirrell DA (1998) Reversible hydrogels from self-assembling artificial proteins. *Science (80-)* 281(5375):389–392.
5. Ichimura K (2000) Photoalignment of liquid-crystal systems. *Chem Rev* 100(5):1847–1874.
6. Kato T, Mizoshita N, Kishimoto K (2006) Functional liquid-crystalline assemblies: self-organized soft materials. *Angew Chemie Int Ed* 45(1):38–68.
7. Musevic I, Skarabot M, Tkalec U, Ravnik M, Zumer S (2006) Two-dimensional nematic colloidal crystals self-assembled by topological defects. *Science (80-)* 313(5789):954–958.
8. Stark H (2001) Physics of colloidal dispersions in nematic liquid crystals. *Phys Rep* 351(6):387–474.
9. Nastishin Y, et al. (2005) Optical characterization of the nematic lyotropic chromonic liquid crystals: Light absorption, birefringence, and scalar order parameter. *Phys Rev E* 72(4):041711.
10. Lydon J (2010) Chromonic review. *J Mater Chem* 20(45):10071–10099.
11. Collings PJ, Dickinson AJ, Smith EC (2010) Molecular aggregation and chromonic liquid crystals. *Liq Cryst* 37(6-7):701–710.
12. Jeong J, Davidson ZS, Collings PJ, Lubensky TC, Yodh AG (2014) Chiral symmetry breaking and surface faceting in chromonic liquid crystal droplets with giant elastic anisotropy. *Proc Natl Acad Sci U S A* 111(5):1742–7.
13. Jeong J, et al. (2015) Chiral structures from achiral liquid crystals in cylindrical capillaries. *Proc Natl Acad Sci* 112(15):E1837–E1844.
14. Nych A, et al. (2014) Chiral bipolar colloids from nonchiral chromonic liquid crystals. *Phys Rev E* 89(6):062502.
15. Mushenheim PC, et al. (2015) Effects of confinement, surface-induced orientations and strain on dynamical behaviors of bacteria in thin liquid crystalline films. *Soft Matter* 11(34):6821–6831.
16. Yamashita Y, Oka M, Tananka T, Yamazaki M (2002) A new method for the preparation of giant liposomes in high salt concentrations and growth of protein microcrystals in them. *Biochim Biophys Acta* 1561:129–134.
17. Marsh D, Bartucci R, Sportelli L (2003) Lipid membranes with grafted polymers: Physicochemical aspects. *Biochim Biophys Acta - Biomembr* 1615(1-2):33–59.

18. Rawicz W, Olbrich KC, McIntosh T, Needham D, Evans E (2000) Effect of Chain Length and Unsaturation on Elasticity of Lipid Bilayers. *Biophys J* 79(1):328–339.
19. Prinsen P, van der Schoot P (2003) Shape and director-field transformation of tactoids. *Phys Rev E Stat Nonlin Soft Matter Phys* 68(2 Pt 1):021701.
20. Zhou S, et al. (2014) Elasticity, Viscosity, and Orientational Fluctuations of a Lyotropic Chromonic Nematic Liquid Crystal. *Soft Matter* 10:6571–6581.
21. Idiart MA, Levin Y (2004) Rupture of a liposomal vesicle. *Phys Rev E Stat Nonlin Soft Matter Phys* 69(6 Pt 1):061922.
22. Kim Y-K, Shiyanovskii S V, Lavrentovich OD (2013) Morphogenesis of defects and tactoids during isotropic-nematic phase transition in self-assembled lyotropic chromonic liquid crystals. *J Phys Condens Matter* 25:404202.
23. Williams RD (1986) Two transitions in tangentially anchored nematic droplets. *J Phys A Math Gen* 19(16):3211–3222.
24. Zhou S, et al. (2012) Elasticity of lyotropic chromonic liquid crystals probed by director reorientation in a magnetic field. *Phys Rev Lett* 109(3):1–5.
25. Drzaic PS (1995) *Liquid crystal dispersions* (World Scientific).
26. Fernández-Nieves A, Link DR, Marquez M, Weitz DA (2007) Topological changes in bipolar nematic droplets under flow. *Phys Rev Lett* 98(8):87801.
27. Olbrich K, Rawicz W, Needham D, Evans E (2000) Water Permeability and Mechanical Strength of Polyunsaturated Lipid Bilayers. *Biophys J* 79(1):321–327.
28. Marmottant P, Biben T, Hilgenfeldt S (2008) Deformation and rupture of lipid vesicles in the strong shear flow generated by ultrasound-driven microbubbles. *Proc R Soc A* 464(2095):1781–1800.
29. Ohno M, Hamada T, Takiguchi K, Homma M (2009) Dynamic behavior of giant liposomes at desired osmotic pressures. *Langmuir* 25(19):11680–11685.
30. Kaznacheev A V, Bogdanov MM, Taraskin SA (2002) The nature of prolate shape of tactoids in lyotropic inorganic liquid crystals. *J Exp Theor Phys* 95(1):57–63.
31. Varghese N, et al. (2012) Emulsion of aqueous-based nonspherical droplets in aqueous solutions by single-chain surfactants: templated assembly by nonamphiphilic lyotropic liquid crystals in water. *Langmuir* 28(29):10797–807.
32. Simon KA, Sejwal P, Gerecht RB, Luk Y-Y (2007) Water-in-water emulsions stabilized by non-amphiphilic interactions: polymer-dispersed lyotropic liquid crystals. *Langmuir* 23(3):1453–8.
33. Tortora L, et al. (2010) Self-assembly, condensation, and order in aqueous lyotropic chromonic liquid crystals crowded with additives. *Soft Matter* 6(17):4157–4167.
34. Knorr RL, Staykova M (2010) Wrinkling and electroporation of giant vesicles in the gel phase. *Soft Matter* 6(9):1990–1996.
35. Hohlfeld E, Davidovitch B (2015) Sheet on a deformable sphere: Wrinkle patterns suppress curvature-induced delamination. *Phys Rev E* 91(1):12407.
36. Mui BL-S, Dobereiner H-G, Madden TD, Cullis P (1995) Influence of Transbilayer Area

Asymmetry on the Morphology of Large Unilamellar Vesicles. *Biophys Jorunal* 69(September):930–941.

37. Bagatolli LA, Parasassi T, Gratton E (2000) Giant phospholipid vesicles: comparison among the whole lipid sample characteristics using different preparation methods: a two photon fluorescence microscopy study. *Chem Phys Lipids* 105(2):135–147.
38. Sorre B, et al. (2012) Nature of curvature coupling of amphiphysin with membranes depends on its bound density. *Proc Natl Acad Sci U S A* 109(1):173–8.
39. Bar-Ziv R, Moses E (1994) Instability and Pearling States Produced in Tubular Membranes by Competition of Curvature and Tension. *Phys Rev Lett* 73(10):1392–1395.
40. Dobereiner H-G, et al. (1997) Mapping vesicle shapes into the phase diagram: a comparison of experiment and theory. *Phys Rev E* 55(4):4458.
41. Evans E (1991) Entropy-driven tension in vesicle membranes and unbinding of adherent vesicles. *Langmuir* 7(9):1900–1908.
42. Agra-Kooijman DM, et al. (2014) Columnar molecular aggregation in the aqueous solutions of disodium cromoglycate. *Phys Rev E* 89(6):062504.
43. DeGennes PG, Prost J (1994) *The Physics of Liquid Crystals* (Clarendon, Oxford).
44. Peskin CS (2002) The immersed boundary method. *Acta Numer* 11:479–517.
45. Broyden CG (1965) A class of methods for solving nonlinear simultaneous equations. *Math Comput*:577–593.
46. Lavrentovich OD (1998) Topological defects in dispersed words and worlds around liquid crystals, or liquid crystal drops. *Liq Cryst* 24(1):117–126.
47. Prinsen P, Van Der Schoot P (2004) Continuous director-field transformation of nematic tactoids. *Eur Phys J E* 13(1):35–41.
48. Prinsen P, Van Der Schoot P (2004) Parity breaking in nematic tactoids. *J Phys Condens Matter* 16(49):8835.
49. Niggemann G, Kummrow M, Helfrich W (1995) The Bending Rigidity of Phosphatidylcholine Bilayers - Dependences on Experimental-Method, Sample Cell Sealing and Temperature. *J Phys II* 5(3):413–425.
50. Tortora L, Lavrentovich OD (2011) Chiral symmetry breaking by spatial confinement in tactoidal droplets of lyotropic chromonic liquid crystals. *Proc Natl Acad Sci U S A* 108(13):5163–5168.
51. Jamali V, et al. (2015) Experimental realization of crossover in shape and director field of nematic tactoids. *Phys Rev E* 91(4):42507.